University of Birmingham
Research at Birmingham

Computational Investigation of Copper Phosphides as Conversion Anodes for Lithium-Ion Batteries

Harper, Angela F.; Evans, Matthew L.; Morris, Andrew J.

DOI:
10.1021/acs.chemmater.0c02054

License:
Creative Commons: Attribution (CC BY)

Document Version
Publisher's PDF, also known as Version of record

Citation for published version (Harvard):
Harper, AF, Evans, ML & Morris, AJ 2020, 'Computational Investigation of Copper Phosphides as Conversion Anodes for Lithium-Ion Batteries', *Chemistry of Materials*, vol. 32, no. 15, pp. 6629–6639. https://doi.org/10.1021/acs.chemmater.0c02054

Link to publication on Research at Birmingham portal

General rights
Unless a licence is specified above, all rights (including copyright and moral rights) in this document are retained by the authors and/or the copyright holders. The express permission of the copyright holder must be obtained for any use of this material other than for purposes permitted by law.

•Users may freely distribute the URL that is used to identify this publication.
•Users may download and/or print one copy of the publication from the University of Birmingham research portal for the purpose of private study or non-commercial research.
•User may use extracts from the document in line with the concept of 'fair dealing' under the Copyright, Designs and Patents Act 1988 (?)
•Users may not further distribute the material nor use it for the purposes of commercial gain.

Where a licence is displayed above, please note the terms and conditions of the licence govern your use of this document.

When citing, please reference the published version.

Take down policy
While the University of Birmingham exercises care and attention in making items available there are rare occasions when an item has been uploaded in error or has been deemed to be commercially or otherwise sensitive.

If you believe that this is the case for this document, please contact UBIRA@lists.bham.ac.uk providing details and we will remove access to the work immediately and investigate.

Download date: 19. Apr. 2024

CHEMISTRY OF MATERIALS

pubs.acs.org/cm

Article

Computational Investigation of Copper Phosphides as Conversion Anodes for Lithium-Ion Batteries

Angela F. Harper, Matthew L. Evans, and Andrew J. Morris*

Cite This: *Chem. Mater.* 2020, 32, 6629−6639

Read Online

ACCESS | Metrics & More | Article Recommendations | Supporting Information

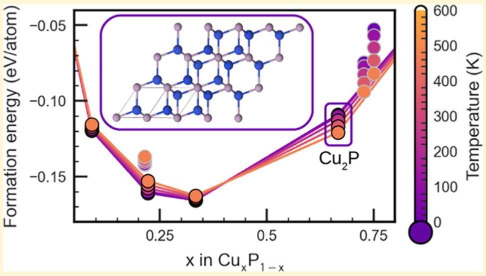

ABSTRACT: Using first-principles structure searching with density-functional theory (DFT), we identify a novel *Fm*$\bar{3}$*m* phase of Cu_2P and two low-lying metastable structures, an *I*$\bar{4}$3*d*−Cu_3P phase and a *Cm*−Cu_3P_{11} phase. The computed pair distribution function of the novel *Cm*−Cu_3P_{11} phase shows its structural similarity to the experimentally identified *Cm*−Cu_2P_7 phase. The relative stability of all Cu−P phases at finite temperatures is determined by calculating the Gibbs free energy using vibrational effects from phonon modes at 0 K. From this, a finite-temperature convex hull is created, on which *Fm*$\bar{3}$*m*−Cu_2P is dynamically stable and the $Cu_{3-x}P$ ($x < 1$) defect phase *Cmc*2_1−Cu_8P_3 remains metastable (within 20 meV/atom of the convex hull) across a temperature range from 0 to 600 K. Both CuP_2 and Cu_3P exhibit theoretical gravimetric capacities higher than contemporary graphite anodes for Li-ion batteries; the predicted Cu_2P phase has a theoretical gravimetric capacity of 508 mAh/g as a Li-ion battery electrode, greater than both Cu_3P (363 mAh/g) and graphite (372 mAh/g). Cu_2P is also predicted to be both nonmagnetic and metallic, which should promote efficient electron transfer in the anode. Cu_2P's favorable properties as a metallic, high-capacity material suggest its use as a future conversion anode for Li-ion batteries; with a volume expansion of 99% during complete cycling, Cu_2P anodes could be more durable than other conversion anodes in the Cu−P system, with volume expansions greater than 150%. The structures and figures presented in this paper, and the code used to generate them, can be interactively explored online using Binder.

■ INTRODUCTION

Graphite is the most commonly employed lithium-ion battery (LIB) anode but is inherently limited by a maximum theoretical capacity of 372 mAh/g upon the formation of LiC_6. Phosphorus (black or red) has a significantly higher theoretical capacity of 2596 mAh/g due to the formation of Li_3P; however, it suffers from capacity deterioration, primarily caused by deleterious volume expansion that occurs upon charging, which constrains the capacity to 350−500 mAh/g in a limited voltage window.[1] In addition, P and its lithiated phases have limited electrical conductivity, requiring dopants and additives to improve performance. By adding transition metals to P, through nanostructuring or synthesis, both electrical conductivity and stability during cycling can be enhanced.[2]

Transition-metal phosphides (TMPs) provide a large design space in which to engineer such high-capacity, conversion anodes for LIBs.[3] High-throughput computational screening has previously identified TMPs with high capacities for LIB electrodes, including TiP, Co_2P, Mn_2P, and others.[4] As conversion anodes for LIBs, TMPs offer both the added gravimetric capacity (ranging from 500 to 2000 mAh/g[4]) and stability against volume expansion over several battery cycles.[5] In addition to bulk or powdered TMPs being used as LIB conversion anodes,[6] nanostructured TMPs can often display improved electrochemical cycling performance.[7] Despite these efforts, TMPs have yet to be widely adopted as conversion anodes, given the large volume expansion (between 150 and 300%[4]) exhibited by anodes with high P content, which limits their cyclability. Despite this drawback in volume expansion, TMPs show higher average voltages than graphite, which has an average voltage of 0.1 V. For example, CoP has an average voltage of 0.67 V, the ternary metal phosphide LiFeP has an average voltage of 0.4 V, and MnP has an average voltage of 0.62 V.[4] Higher average voltages give the metal phosphides improved safety while sacrificing energy density, making them an ideal choice for large-scale and long-term energy storage.

Several previously studied TMP anodes include $FeP_{x=1,2,4}$,[8] Fe_2P nanoparticles,[9] Ni_2P,[10] CuP_2,[11,12] and Cu_3P,[13,14] among others. Of the TMPs tested as conversion anodes, the copper phosphides (specifically CuP_2 and Cu_3P) have shown promise for their cyclability and capacity. The copper phosphides offer additional benefits to the other TMPs, as Cu is already used as a common current collector, providing further cycling capability and resistance to degradation.[15] Cu_3P prepared by high-temperature synthesis had a first-cycle capacity of 527 mAh/g,[13] and a porous Cu_3P anode synthesized by facile

Received: May 15, 2020
Revised: June 24, 2020
Published: June 25, 2020

ACS Publications

https://dx.doi.org/10.1021/acs.chemmater.0c02054
Chem. Mater. 2020, 32, 6629−6639

chemical corrosion exhibited a capacity between 360 and 380 mAh/g over 70 cycles.[16] The capacity of high-temperature-synthesized Cu_3P exceeds that of graphite, and the cyclability of porous Cu_3P is improved relative to other Cu_3P anodes.[13,17] CuP_2, on the other hand, delivers a higher initial capacity of 815 mAh/g, but can only be cycled stably 10 times before the capacity fades to 360 mAh/g.[12] The main factor in this degradation is the high concentration of P in the CuP_2, which, while enabling high capacity, also contributes to the structural instability of CuP_2 during cycling as the lithium-rich Li_3P phase forms. To optimize the trade-off between stability and capacity, it would be beneficial to discover a compound with higher P content than Cu_3P to offer higher capacity, and with a Cu content higher than CuP_2 to aid in cyclability.

By performing crystal structure prediction, combining both ab initio random structure searching (AIRSS) and a genetic algorithm (GA), in addition to structural prototyping with known crystal structures of related chemistries,[18−20] we produced the compositional phase diagram of the copper phosphide system. We describe this approach to structure prediction and the application of open-source Python packages `matador` (v0.9),[21] for high-throughput first-principles calculations, and `ilustrado` (v0.3),[22] for computational structure prediction with GAs. Crystal structure prediction for battery anodes is a well-tested method,[23] used for identifying both novel anode materials[4] and unknown phases, which form during battery cycling.[24,25] AIRSS has been used previously to search for additional phases of Li−P and Na−P, which form during battery cycling.[26] The GA was also employed to search for new phases of Na−P, which were confirmed experimentally by solid-state NMR spectroscopy.[27] As applied here to Cu−P, these methods predict a novel metallic $Fm\bar{3}m$−Cu_2P phase at 0 K, within the target composition range of $Cu_{1<x<3}P$, for a high-capacity, low-volume expansion conversion anode; we compare its electronic structure to other TMPs to show a similarity to $Fm\bar{3}m$−Rh_2P and $Fm\bar{3}m$−Ir_2P. Two other phases, Cm−Cu_3P_{11} and $I\bar{4}3d$−Cu_3P, are identified as metastable, both bearing structural similarity to known copper phosphides. We calculate the convex hull of Cu−P at temperatures up to 600 K, confirming the dynamic and chemical stabilities of Cu_2P across this temperature range. A ground-state voltage profile from density-functional theory (DFT) shows that $Fm\bar{3}m$−Cu_2P undergoes the same lithiation process as $P6_3cm$−Cu_3P; however, $Fm\bar{3}m$−Cu_2P has a higher capacity of 508 mAh/g, with an average voltage of 0.86 V versus Li/Li^+ (compared to 0.91 V for $P6_3cm$−Cu_3P).

■ METHODS

To search for novel copper phosphides, we first performed structural relaxations of the 13 structures from the Inorganic Crystal Structure Database (ICSD)[28] of Cu_xP ($0 < x < 1$). The Python package `matador`[21] was used to query 1053 prototype binary structures from the Open Quantum Materials Database (OQMD),[19] with chemical compositions containing a pnictogen and a transition metal from the first two rows, namely, {Ti, V, Cr, Mn, Fe, Co, Ni, Cu, Zn, Zr, Nb, Mo, Tc, Ru, Rh, Pd, Ag, Cd}−{P, As, Sb}; each composition was then transmuted to the corresponding stoichiometry of Cu−P, yielding 909 unique structures after geometry optimization. To extend this search beyond existing prototypes, two additional structure prediction steps were performed, namely, AIRSS[29] and an evolutionary search with the GA implemented in the `ilustrado`[22] package.

When performing AIRSS, one proceeds by generating random "sensible" (symmetry, density, and atomic separation constrained) trial cells and then geometry-optimizing them to their corresponding local minima. All relaxations can be performed concurrently, with no interdependence between calculations. New trial structures are generated until the ground state of each stoichiometry (within the constraints of the search) has been found multiple times.

We initially performed an exploratory AIRSS search consisting of around 5000 trial structures, with constraints on cell size, stoichiometry, and number of atoms in the cell. In this initial search, the total number of atoms in the cell was constrained to be ≤40, and the total number of formula units was randomized between 1 and 4, while still keeping the total number of atoms below 40. The number of atoms of Cu and P were randomized between 1 and 9 in each cell, and the cell volume (V) was constrained based on the total number of atoms in the cell (N) to be $8N\,Å^3 \leq V \leq 20N\,Å^3$, based on the average densities of Cu−P phases within the ICSD.

Structures from the searching and enumeration procedures were then used, with fitness weighted according to their distance from the convex hull, as the initial configurations for a GA implemented in the Python package `ilustrado`.[22] The `ilustrado` package uses a simple cut-and-splice crossover operation, supplemented by mutation operators (random noise, atomic permutations, vacancies, and adatoms).[30] To avoid stagnation, each trial structure was filtered for similarity (via pair distribution function, PDF, overlap) against existing structures in the population. Three independent GA runs were performed with 10 generations each, yielding a further 1049 relaxed structures. Finally, a directed AIRSS search of Cu_xP_y, where $x + y < 8$, was performed to create a final set of ∼20 000 structures within the Cu−P chemical space. In all cases, to constrain the search to physically reasonable structures, a minimum atomic separation of 1.5 Å was enforced and the maximum number of atoms in the cell was constrained to 10 for the initial ∼10 000 AIRSS searches and 40 atoms per cell for the final ∼3000 trials.

All calculations were performed using CASTEP (v18.1 and v19.1), the plane wave pseudopotential DFT package.[31] To maximize computational efficiency, the initial calculations were performed with loose convergence criteria that ensured formation energies converged to 10 meV/atom. The Perdew−Burke−Ernzerhof (PBE) exchange−correlation functional was used[32] with Vanderbilt ultrasoft pseudopotentials[33] that required a plane wave kinetic energy cutoff of 300 eV to converge energies to within 10 meV/atom. The Brillouin zone (BZ) was sampled with a Monkhorst−Pack grid k-point spacing finer than $2\pi \times 0.05\ Å^{-1}$; the grid was frequently recomputed to accommodate any changes in the cell shape and size during relaxation. Each structure was geometry-optimized at this accuracy to a force tolerance of 0.05 eV/Å. The structures with a formation energy within 50 meV of the convex hull were then further optimized once more using CASTEP's on-the-fly (OTF) "C18" library of ultrasoft pseudopotentials,[a] with a finer k-point sampling of $2\pi \times 0.03\ Å^{-1}$ and plane wave kinetic energy cutoff of 500 eV, which yielded formation energies converged to within 2.5 meV/atom. To predict the voltage profiles with the same convergence criteria (formation energies within 2.5 meV/atom), the relaxation of known Li−P structures required a higher plane wave cutoff of 700 eV. Therefore, to compare ternary phases of Cu−Li−P in the voltage profile, all Cu−Li−P phases were reoptimized at a plane wave kinetic energy cutoff of 700 eV.

To identify stable structures from this search, a convex hull of the copper phosphides was created. The formation energy E_f of each structure Cu_xP_y was calculated using

$$E_f(Cu_xP_y) = E(Cu_xP_y) - xE(Cu) - yE(P) \quad (1)$$

where $E(Cu)$ is the DFT total energy of the $Fm\bar{3}m$−Cu structure, and $E(P)$ is the energy of $Cmca$-P (black phosphorus). Black phosphorus was used as the P chemical potential instead of the lower-energy polymorph red phosphorus; as has been previously discussed in Mayo et al.,[26] black phosphorus is commonly used when making electrochemical cells.[34]

Electrochemical voltage profiles for Li insertion into the stable Cu−P phases were calculated from the computed formation energies from the ternary convex hull of Cu−Li−P. To calculate the voltage profiles shown in the Cu_2P as a Li-Ion Battery Conversion Anode section, the voltage, $\bar{V}$, between two tie-lines in the ternary convex hull with compositions $\mathrm{Li}_{x_1}\mathrm{Cu}_n\mathrm{P}$ and $\mathrm{Li}_{x_2}\mathrm{Cu}_n\mathrm{P}$ was calculated using

$$\bar{V}(x_1, x_2) = -\frac{E(\mathrm{Li}_{x_1}\mathrm{Cu}_n\mathrm{P}) - E(\mathrm{Li}_{x_2}\mathrm{Cu}_n\mathrm{P}) - (x_1 - x_2)E(\mathrm{Li})}{(x_1 - x_2)F} \tag{2}$$

as stated by Urban et al.[35] In eq 2, $E(\mathrm{Li}_{x_1}\mathrm{Cu}_n\mathrm{P})$ and $E(\mathrm{Li}_{x_2}\mathrm{Cu}_n\mathrm{P})$ are the ground-state energies of two phases along the reaction pathway of the ternary convex hull, in which x_1 and x_2 are the relative amounts of Li in the starting and ending products at each point in the pathway.

All phonon calculations were performed under the harmonic approximation with the PBE *xc*-functional in a 2 × 2 × 2 supercell (corresponding to a phonon *q*-point spacing of $2\pi \times 0.046$ Å^{-1} for $Fm\bar{3}m-\mathrm{Cu_2P}$) using the finite displacement method implemented in the CASTEP code. The dynamical matrix was then Fourier-interpolated onto the BZ path provided by the SeeK-path Python package[36,37] to compute the phonon dispersion and onto a fine Monkhorst–Pack grid to compute the phonon density of states.

The band structure for $\mathrm{Cu_2P}$ was calculated using the higher accuracy parameters and pseudopotentials mentioned previously, and the electronic density of states was integrated and projected onto atomic orbitals using the OptaDOS code.[38,39] Vibrational properties of all stable phases were computed using the finite displacement method, with an added many-body dispersion (MBD denoted MBD* in CASTEP v19.0) correction[40] to account for interlayer interactions in black phosphorus.

The open-source Python package `matador` (v0.9)[21] was used to run the CASTEP calculations, perform the analysis, and create the plots found in this article. All of this analysis, as well as the underlying source code and data, can be explored interactively using Binder and is found on GitHub at harpaf13/data.copper-phosphides. The input and output files associated with our calculations have been deposited into the Cambridge Repository at https://doi.org/10.17863/CAM.54795.

■ RESULTS

From the search of ∼20 000 trial structures, there are 42 unique phases within 50 meV/atom of the convex hull. Previous computational structure searches have used a distance above the hull of 25 meV/atom,[41] and given the accuracy of PBE,[42] we chose to increase this cutoff to 50 meV/atom. Furthermore, the experimentally verified $P6_3cm-\mathrm{Cu_3P}$ structure[43] is 37 meV/atom above the convex hull tie-line, further justifying this cutoff. The uniqueness was determined by computing pairwise overlap integrals of the pair distribution functions of phases at each stoichiometry using `matador`. The set of 42 unique phases contains four experimentally reported copper phosphides from the ICSD: $P\bar{1}-\mathrm{CuP_{10}}$ synthesized by a mineralization reaction[44] and $C2/m-\mathrm{Cu_2P_7}$,[45] $P2_1/c-\mathrm{CuP_2}$[4545] and $P6_3cm-\mathrm{Cu_3P}$[43,46] from high-temperature sintering.

Oloffson's experiments on single-crystal $P6_3cm-\mathrm{Cu_3P}$ synthesized at high temperature, and subsequent work by De Trizio et al.,[47] show that $\mathrm{Cu_3P}$ has several defects[43] with a range of stoichiometries between $\mathrm{Cu_{2.6}P}$ and $\mathrm{Cu_{2.8}P}$. DFT studies of the Cu vacancies indicate that $\mathrm{Cu_3P}$ is substoichiometric,[47] and to search this substoichiometric space, unit cells of $P6_3cm-\mathrm{Cu_{18}P_6}$ were enumerated with 1, 2, and 3 Cu vacancies, resulting in 76 $\mathrm{Cu_{3-x}P}$ structures. The lowest-energy defect was a $Cmc2_1-\mathrm{Cu_8P_3}$ ($\mathrm{Cu_{2.67}P}$) phase 26 meV/atom above the convex hull tie-line, denoted as vacancy enumeration in Figure 1.

The convex hull of Cu–P, with points colored by the provenance of each structure, is presented in Figure 1; the experimentally identified phases, and a new $Fm\bar{3}m-\mathrm{Cu_2P}$ phase, all lie on the convex hull tie-line and are each labeled with an arrow.

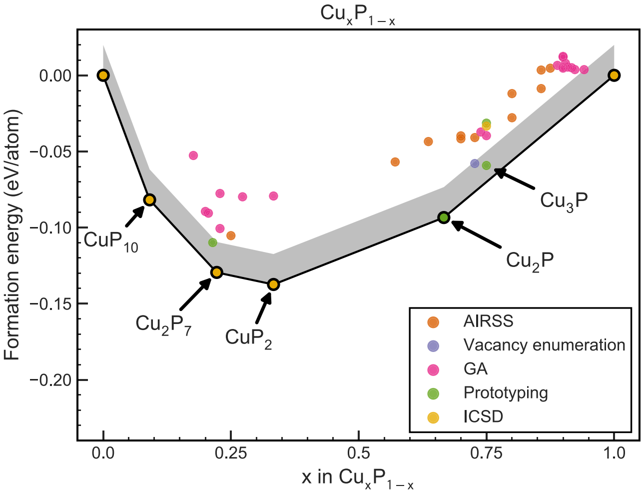

Figure 1. Convex hull of Cu–P phases from structure searching. Four structures lie on the convex hull: $\mathrm{CuP_{10}}$, $\mathrm{Cu_2P_7}$, $\mathrm{CuP_2}$, and $\mathrm{Cu_2P}$. Structures are colored according to their provenance: either from a searching method (AIRSS, GA, prototyping, vacancy enumeration) or from an existing database (ICSD). Prototyping refers to using a prototype structure from the ICSD and replacing the atoms with Cu or P, as described in the Methods section. The vacancy enumeration phases are the phases optimized after adding Cu vacancies to $P6_3cm-\mathrm{Cu_3P}$. Phases within 20 meV/atom of the convex hull lie within the shaded gray region, and $\mathrm{Cu_3P}$ is labeled for reference.

Details of the 24 structures, which are both negative in the formation energy relative to Cu and P and are within 50 meV/atom of the convex hull, are given in Table 1. Phases on the convex hull tie-line in Figure 1 are indicated with an asterisk in Table 1, and phases that are experimentally confirmed are denoted by their ICSD Collection Code as "ICSD #". Phases not reported previously, within 20 meV/atom of the convex hull tie-line, are bolded in Table 1. The provenance of each phase is given in the last column of Table 1. Phases that were found by swapping the elements of a prototype ICSD structure are denoted by the ICSD Collection Code of the prototype used as "prototype #".

Of the 24 binary structures in Table 1, 9 were discovered by AIRSS, 6 by the GA, 4 from structural prototyping, and 4 were previously known Cu–P structures from the ICSD. Of particular interest are three new phases, bolded in Table 1, $Fm\bar{3}m-\mathrm{Cu_2P}$, $I\bar{4}3d-\mathrm{Cu_3P}$, and $Cm-\mathrm{Cu_3P_{11}}$, which are all within 20 meV/atom of the convex hull and will be discussed further in the following sections.

Phosphorus-Rich Phase $Cm-\mathrm{Cu_3P_{11}}$. $Cm-\mathrm{Cu_3P_{11}}$ is a new structure that was found by relaxing the prototype $\mathrm{Ag_3P_{11}}$ (ICSD 26563); it is 17 meV/atom from the hull tie-line and has structural similarity to the ICSD structure $C2/m-\mathrm{Cu_2P_7}$ (ICSD 35281),[45] as shown in Figure 2. Both of these structures have repeating chains of P atoms, as seen in the supercells in Figure 2, in which alternating patterns of Cu or Cu–P are connected to a zig-zag chain of P atoms. All known phases in the P-rich ($\mathrm{Cu_xP}$, where $x > 1$) region of the convex hull, namely, $C2/m-\mathrm{Cu_2P_7}$ (ICSD 35281),[45] $P2_1/c-\mathrm{CuP_2}$ (ICSD 35281),[45] and $P\bar{1}-\mathrm{CuP_{10}}$ (ICSD 418805),[44] have long chains of P atoms, similar to the layered $P2/c$-P (ICSD 29273,[54] red P).

In the P-rich region, five new phases were identified within 50 meV/atom of the convex hull: $Pmmn-\mathrm{CuP_3}$, $Cm-\mathrm{Cu_8P_{27}}$, $Cm-\mathrm{Cu_3P_{11}}$, $Cm-\mathrm{Cu_7P_{27}}$, and $Cm-\mathrm{CuP_4}$. Using the GA, it was possible to include structures with stoichiometries of P up to

Table 1. Phases of Cu−P with a Formation Energy $\leq$ 0 meV/atom Relative to Cu and P and the Distance from the Convex Hull Tie-Line, ΔE, Less Than 50 meV/atom

formula	on tie-line	ΔE (meV/atom)	space group	provenance
Cu	*		$Fm\bar{3}m$	ICSD 43493[a]
Cu_6P		31	$I4/mmm$	AIRSS
Cu_4P		28	$P4/nmm$	AIRSS
Cu_4P		44	$Cmmm$	AIRSS
Cu_3P		**11**	**$I\bar{4}3d$**	**prototype 64715**[b]
Cu_3P		30	$P2_1/m$	GA
Cu_3P		37	$P6_3cm$	ICSD 15056[c]
Cu_3P		39	$I\bar{4}$	prototype 23560[d]
$Cu_{17}P_6$		40	$P1$	GA
Cu_8P_3		26	$Cmc2_1$	AIRSS
Cu_8P_3		36	$P6_3cm$	AIRSS
Cu_8P_3		39	$P1$	AIRSS
Cu_7P_3		42	$P1$	AIRSS
Cu_7P_3		44	$P1$	AIRSS
Cu_2P	*		**$Fm\bar{3}m$**	**prototype 38356**[e]
Cu_4P_3		49	$P4/nmm$	AIRSS
CuP_2	*		$P2_1/c$	ICSD 35282[f]
CuP_3		26	$Pmmn$	AIRSS
Cu_8P_{27}		29	Cm	GA
Cu_8P_{27}		43	Cm	GA
Cu_2P_7	*	-	$C2/m$	ICSD 35281[g]
Cu_3P_{11}		**17**	**Cm**	**prototype 26563**[h]
Cu_7P_{27}		33	Cm	GA
CuP_4		32	Cm	GA
CuP_{10}	*		$P\bar{1}$	ICSD 418805[i]
P	*		$Cmca$	ICSD 150873[j]

Bold text indicates new phases with $\Delta E \leq 20$ meV/atom. [a]Experimental lattice parameter for Cu from ref 48. [b]Prototype structure is $I\bar{4}3d-Cu_3As$.[49] [c]Structure from single-crystal diffractometry.[43] [d]Prototype structure $I\bar{4}-Cr_3P$ by single-crystal X-ray diffraction.[50] [e]Prototype structure $Fm\bar{3}m-Rh_2P$ by X-ray diffraction.[51] [f]Structure from X-ray diffraction.[45] [g]Structure from X-ray diffraction.[45] [h]Prototype structure $Cm-Ag_3P_{11}$ by single-crystal X-ray diffraction.[52] [i]Structure from single-crystal X-ray diffraction.[44] [j]Black phosphorus structure from powder X-ray diffraction.[53]

27 atoms in the unit cell and thus found structural variations on Cu_2P_7 such as Cu_3P_{11}. To compare the new metastable $Cm-Cu_3P_{11}$ structure with other P-rich structures, the pair distribution functions (PDFs) and calculated powder X-ray diffraction (PXRD) peaks of CuP_2, Cu_2P_7, and Cu_3P_{11} were calculated and are compared in Figure 3. In all three cases, the initial sharp peak in the PDF between 2.20 and 2.24 Å shows, unsurprisingly, the same Cu−P and P−P distances shared by all three structures. The peaks at radii above 3 Å show the longer-range similarity between Cu_3P_{11} and Cu_2P_7, which is not shared by CuP_2. Comparison of the PXRD patterns of $C2/m-Cu_2P_7$ and $Cm-Cu_3P_{11}$ shows that $Cm-Cu_3P_{11}$ is distinguished by a peak at a 2θ value of 16°, where $C2/m-Cu_2P_7$ has an indistinguishable peak at this point. Given the shared symmetry operations between Cm and $C2/m$, we expect to see peaks at the same 2θ values, but the intensities will vary between the structures. We deduce that these three phases could be verified using experimental PXRD, by using the peaks at $2\theta < 30°$ to distinguish between the phases.

$Cu_{3-x}P$ Phases ($x \leq 1$). Within the stoichiometry range $Cu_{3-x}P$ ($x \leq 1$), four unique Cu_3P phases, $Cu_{17}P_6$, Cu_8P_3, Cu_7P_3, and Cu_2P, were found. Of these, $P6_3cm-Cu_3P$ was the only phase previously experimentally determined and had a formation energy of 37 meV/atom above the convex hull tie-line. Olofsson identified the stoichiometry of $P6_3cm-Cu_3P$ at 975 K to be between $Cu_{2.867}P$ and $Cu_{2.755}P$ due to Cu vacancies within the unit cell of $P6_3cm-Cu_{18}P_6$ (shown in Figure S1).[43] A study on low-temperature phases of $Cu_{3-x}P$ proposes phases from $Cu_{2.3}P$ to $Cu_{2.9}P$.[55] The lowest-energy $Cu_{3-x}P$ ($x \leq 1$) phases identified in Table 1, $P1-Cu_{17}P_6$ ($Cu_{2.83}P$), $Cmc2_1-Cu_8P_3$ ($Cu_{2.66}P$), and $P1-Cu_7P_3$ ($Cu_{2.33}P$), are all defect structures of $P6_3cm-Cu_3P$ with 1, 2, and 4 Cu vacancies respectively, from the $P6_3cm-Cu_{18}P_6$ unit cell of Cu_3P. Of these three $P6_3cm-Cu_3P$ defect structures, $Cmc2_1-Cu_8P_3$ ($Cu_{2.66}P$) has the smallest distance from the hull (ΔE = 26 meV/atom). This corroborates the previous DFT calculations suggesting Cu_3P has two Cu vacancies.[47]

In addition to the ICSD phase of $P6_3cm-Cu_3P$ (ΔE = 37 meV/atom), two other Cu_3P phases were found, which are closer to the convex hull tie-line than $P6_3cm-Cu_3P$; these are the $P2_1/m-Cu_3P$ (ΔE = 30 meV/atom) and $I\bar{4}3d-Cu_3P$ phases (ΔE = 11 meV/atom). The $P2_1/m-Cu_3P$ phase is structurally related to the $Fm\bar{3}m-Cu_2P$ (ΔE = 0 meV/atom) phase (discussed in the following section). These two phases are shown in Figure 4, in which the $P2_1/m-Cu_3P$ can be described as a stacking of the $Fm\bar{3}m-Cu_2P$ phase. While the $Fm\bar{3}m-Cu_2P$ phase has not been observed experimentally, it is likely that the two phases could be distinguished, given their distinct PDF and PXRD patterns shown in Figure S2. The PXRD pattern for $P2_1/m-Cu_3P$ has additional low-intensity peaks to the right of the 46° peaks and is distinct from the other low-energy phases of Cu_3P as shown in Figure S2, which would further distinguish this phase in experiment.

The lowest-energy Cu_3P phase is an $I\bar{4}3d$ phase 11 meV/atom above the tie-line, which was identified by relaxing the prototype $I\bar{4}3d-Cu_3As$ structure (ICSD 64715[49,57]). The $I\bar{4}3d-Cu_3P$ structure is the highest-symmetry Cu_3P phase and is the only cubic phase in the set of low-energy Cu_3P structures. $I\bar{4}3d-Cu_3P$ contains 8 formula units in the primitive unit cell and has 9-fold coordinated P atoms, whereas $P6_3cm-Cu_3P$ has 8-fold coordinated P atoms. The resulting crystal structures, shown in Figure S1, show two different long-range orderings of the Cu subnetwork. $P6_3cm-Cu_3P$ has only one, 8-fold coordinated, P site, which results in continuous zig-zag chains of Cu atoms surrounding the P, which are at the peaks of the buckles in the zig-zag. In $I\bar{4}-Cu_3P$, there are two 9-fold coordinated sites: one site at the center of the surrounding Cu (seen in Figure S1) and one at the edges, which together form a hexagonal Cu cage surrounding the P atom in the center. While both phases have high-coordinated P atoms, the $I\bar{4}3d-Cu_3P$ shows a network of Cu atoms surrounding a central P atom, where $P6_3cm-Cu_3P$ contains infinite Cu chains in the c direction.

Another trigonal phase, $P\bar{3}c1-Cu_3P$ (ICSD 16841,[49] $\Delta E >$ 50 meV/atom), has the same structure as $P\bar{3}c1-Cu_3As$ (ICSD 16840[49]); however, it is 82 meV/atom above the convex hull tie-line. To the best of our knowledge, there are no reports of an $I\bar{4}3d-Cu_3P$ phase, either experimentally or in a computational database. The PDF and PXRD patterns of $I\bar{4}3d-Cu_3P$ given in Figure S2 show no relation to any other Cu_3P phase, or the $Fm\bar{3}m-Cu_2P$ phase; thus, if energetically stable, it could be distinguished using PXRD in the experiment.

$Fm\bar{3}m-Cu_2P$. The $Fm\bar{3}m-Cu_2P$ phase was found from the prototype $Fm\bar{3}m-Ir_2P$ (ICSD 640898).[58] Comparing the Cu_2P phase to both Ir_2P and Rh_2P using PDFs in Figure S3 shows that the PDFs are identical between all three structures, and the

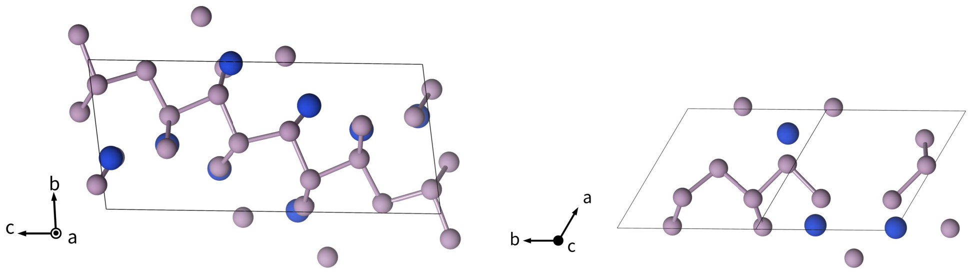

(a) $C2/m$–Cu_2P_7 unit cell (b) Cm–Cu_3P_{11} unit cell

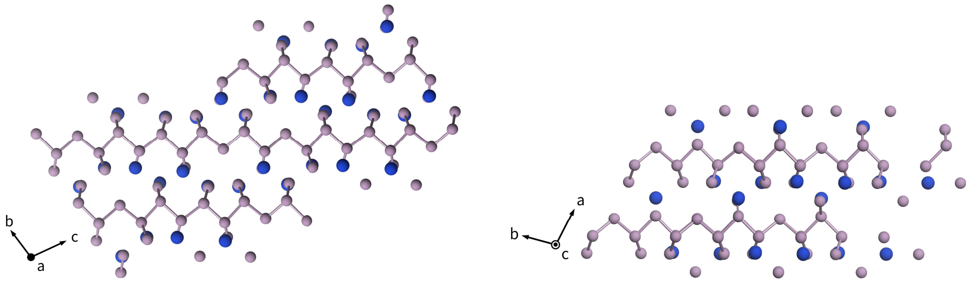

(c) $C2/m$–Cu_2P_7 (d) Cm–Cu_3P_{11}

Figure 2. (a) Cu_2P_7 unit cell, (b) Cu_3P_{11} unit cell, and (c) Cu_2P_7 2 × 2 × 2 supercell in which the P–P connectivity is shown to highlight the P chains in the supercell structure. (d) Cu_3P_{11} 2 × 2 × 2 supercell with the P–P connectivity to show P chains as in the Cu_2P_7 supercell.

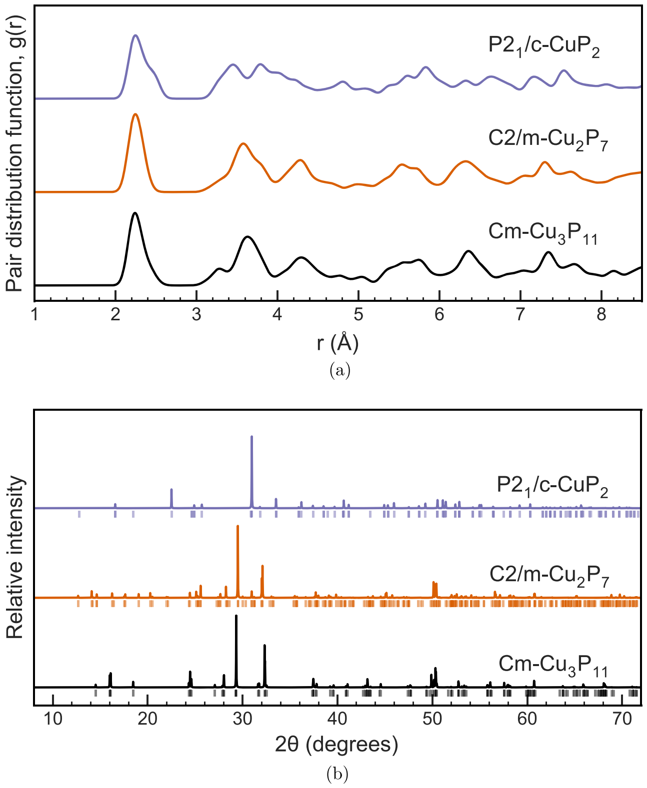

Figure 3. (a) Pair distribution function (PDF) of Cm–Cu_3P_{11}, $P2_1/c$–CuP_2 (ICSD 35282), and $C2/m$–Cu_2P_7 (ICSD 35281) shows all three have a first peak between 2.20 and 2.24 Å, while CuP_2 has two peaks around 3.6 Å, where both Cu_2P_7 and Cu_3P_{11} have one. All PDFs are artificially broadened with Gaussians of width 0.1 Å, and PXRDs are calculated using a Cu Kα source. (b) Simulated PXRD patterns of both Cu_2P_7 and Cu_3P_{11} share peak positions, as is expected from their shared symmetries. The Cu_3P_{11} phase could be identified experimentally by the higher-intensity peaks at $2\theta < 30°$, including a distinct peak at 16°, not present in Cu_2P_7. Details of PXRD calculations can be found in the Supporting Information.

PXRD plot of Cu_2P has the same peaks, all shifted to slightly higher values of 2θ due to structural relaxations in the geometry optimization of Cu_2P.

Previously, a 2D structure of Cu_2P was predicted theoretically as a buckled nonmagnetic material,[56] in which the magnetism expected was inhibited by the buckled layers. The buckled layers from the 2D phase are also present in the bulk $Fm\overline{3}m$–Cu_2P, and the nonmagnetic nature was confirmed in the bulk phase by the lack of spin-polarization in the density of states shown in Figure S4. The bulk $Fm\overline{3}m$–Cu_2P structure described above has the same structural motifs as the 2D hexagonal phase predicted by Yang et al.[56] and has the same electronic properties.

$Fm\overline{3}m$–Cu_2P lies on the convex hull tie-line and is energetically more stable than both the experimentally confirmed phase of $P6_3cm$–Cu_3P and its defect structure $Cmc2_1$–Cu_8P_3. Figure 5 shows the phonon dispersion for the $Fm\overline{3}m$–Cu_2P computed as mentioned in the Methods section. No imaginary phonon frequencies were present in the dynamical matrix (interpolated or otherwise), indicating that $Fm\overline{3}m$–Cu_2P is dynamically stable.

The electronic structure of $Fm\overline{3}m$–Cu_2P is related to the electronic structure of other $Fm\overline{3}m$ TMPs, suggesting that it belongs to the same class of materials as $Fm\overline{3}m$–Ir_2P and Rh_2P. Of the TMPs in the Materials Project database,[59] 21 are insulating and 68 are metallic with a high density of transition-metal d-bands below the Fermi level. Figure 6 shows the electronic band structure and density of states of $Fm\overline{3}m$–Cu_2P projected by species along the high-symmetry path from SeeK-path used previously and the density of states projected by the angular momentum channel on a fine Monkhorst–Pack grid. The band structure shows that Cu_2P is a metal with P and Cu bands touching at the Γ point of ∼2.0 eV above the Fermi level. In addition, there is a characteristic high density of flat bands localized on the Cu ions that exhibit a d-character of around 2.5 eV below the Fermi level. Calculating this band structure using the HSE06 functional (shown in Figure S5), a hybrid functional designed to correct for band-gap underestimation, the gap at Γ between the Cu and P bands is closed.

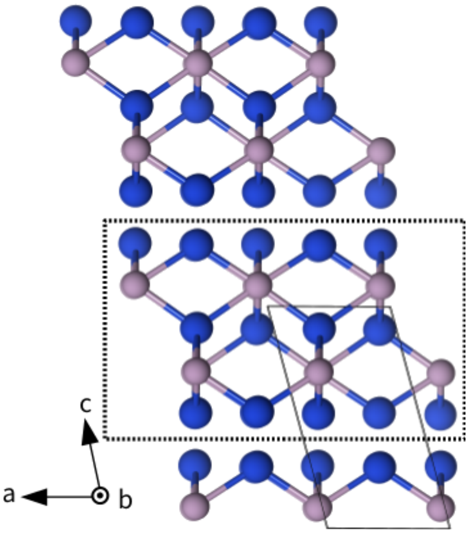

(a) $P2_1/m$–Cu_3P

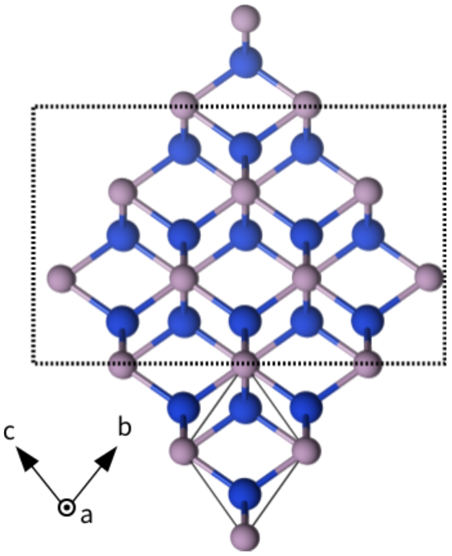

(b) $Fm\bar{3}m$–Cu_2P

Figure 4. $P2_1/m$−Cu_3P found by the GA and $Fm\bar{3}m$−Cu_2P from a swap with $Fm\bar{3}m$−Ir_2P. Here Cu atoms are colored blue and P atoms are colored pink. $P2_1/m$−Cu_3P structure can be described as a stacking of Cu_2P layers separated by Cu atoms. The stacking pattern, which is present in both structures, is indicated by the black dashed line surrounding the atoms in each structure. This is meant to guide the eye and show the similarity in the two structures. The unit cells of each structure are outlined with a thin gray box. Cu_2P is predicted to be a stable two-dimensional (2D) phase,[56] which could be layered to produce the Cu_3P phase shown in panel (a) here.

Many M_2P phases (where M is a transition metal) have a structure similar to $P\bar{6}2m$-‑Ni_2P[60] and Fe_2P,[61,62] in which the metal atoms sit in a cage of 3-fold coordinated P and 4-fold coordinated metal atoms. $Fm\bar{3}m$−Cu_2P is most similar to the other $Fm\bar{3}m$ TMPs, as it was derived from the prototype structure $Fm\bar{3}m$−Ir_2P, and has a 4-fold coordinated Cu with an 8-fold coordinated P. The Cu_2P band structure in Figure 6 is also similar to those of Ir_2P and Rh_2P. In Rh_2P, there is a directionally opened gap of 1 eV above the Fermi level at the Γ point, not present in Cu_2P or Ir_2P (Cu_2P, Ir_2P, and Rh_2P band structures calculated with spin−orbit coupling are given in Figure S6).

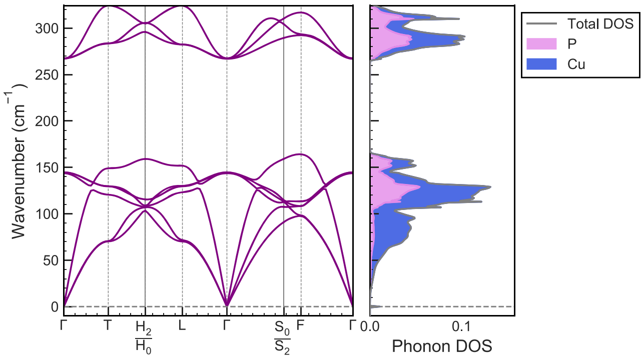

(a)

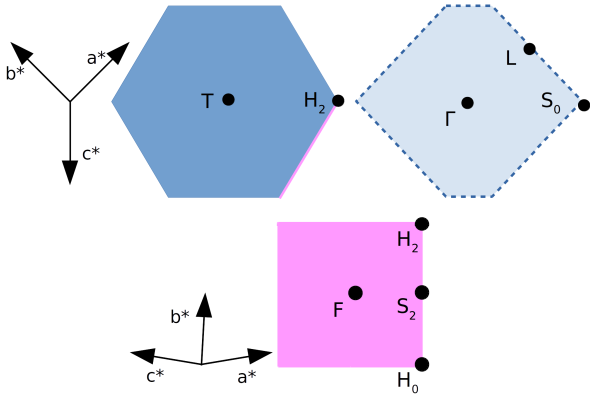

(b)

Figure 5. (a) Cu_2P phonon dispersion under the harmonic approximation and the corresponding Brillouin zone. Phonon dispersion and density of states were interpolated from the dynamical matrix calculated using the PBE *xc*-functional and the C18 pseudopotential library, with a $2\pi \times 0.03$ $Å^{-1}$ *k*-point spacing, 500 eV plane wave cutoff, in a $2 \times 2 \times 2$ supercell using the finite displacement method (corresponding to a phonon *q*-point spacing of $2\pi \times 0.046$ $Å^{-1}$). (b) Brillouin zone is a truncated octahedron, with special points on each face labeled here. The dashed hexagon outline indicates the center of the Brillouin zone.

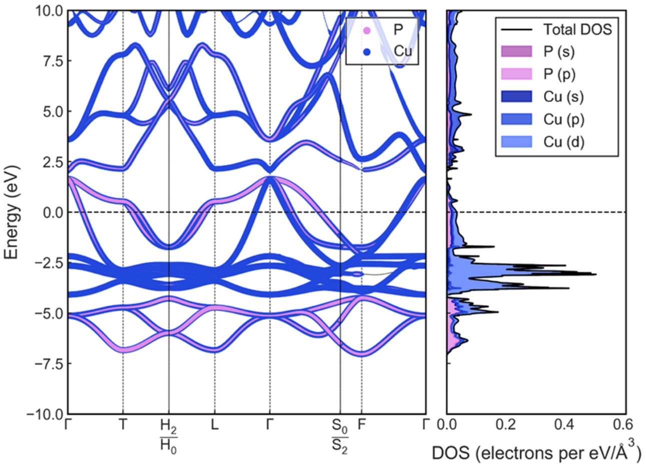

Figure 6. Electronic band structure of Cu_2P projected onto the Cu and P states and density of states projected onto the Cu s, p, d and P s and p states, for Cu_2P using an energy cutoff of 500 eV with a $2\pi \times 0.03$ $Å^{-1}$ *k*-point spacing and C18 on-the-fly pseudopotentials. The projected band structure is produced by OptaDOS,[38] and band energies are calculated by CASTEP.[31]

Both of these structures exhibit spin−orbit coupling due to their heavy metal ions, while Cu has negligible spin−orbit coupling effects. The Rh_2P and Ir_2P band structures are calculated, including spin−orbit coupling.

Finite-Temperature Phase Stability. The temperature-dependent convex hull was constructed by calculating the finite-temperature Gibbs free energies by including vibrational effects at the harmonic level[63] of several related structures on or near the convex hull from Figure 1. All structures within 20 meV/atom of the hull at 0 K were included in the finite-temperature hull; these were $Fm\bar{3}m$−Cu_2P, $I\bar{4}3d$−Cu_3P, $Cmc2_1$−Cu_8P_3 (the structure with 2 Cu vacancies from $P6_3cm$−Cu_3P discussed previously), CuP_2, CuP_{10}, Cu_2P_7, and Cu_3P_{11}.

The chemical potentials for this binary convex hull were *Cmca*-P (black phosphorus) and $Fm\bar{3}m$−Cu. Previously, Mayo et al. noted that the inclusion of semiempirical dispersion corrections for black phosphorus changed the energetics of the convex hull,[26] and therefore, it is not possible to combine optimized structures with and without dispersion corrections on the same convex hull. However, to obtain nonimaginary phonon frequencies of *Cmca*-P, it is necessary to account for dispersion. To account for this, the many-body dispersion correction (MBD) was applied during the geometry optimization and phonon calculation.[40] Using PBE, the distance between P chains in black phosphorus is 3.95 Å. By applying this correction, the P−P chain distance was reduced to 3.58 Å. To include the MBD black phosphorus on the convex hull in Figure 7a, we calculated the free energy of black phosphorus $F(T)$ at a given temperature T as

$$F(T) = H + \Delta F^{\mathrm{MBD}*}(T) \tag{3}$$

where H is the enthalpy without the dispersion correction, and $\Delta F^{\mathrm{MBD}*}(T)$ is the free-energy contribution at temperature T with the MBD dispersion correction, which includes the zero-point energy. In this way, the energies of black phosphorus were referenced to the ground-state energy without dispersion. The SCAN functional accurately describes the phonon modes of black phosphorus without any added dispersion corrections (i.e., no imaginary modes are observed) and therefore is used as a comparison to the MBD-corrected PBE functional in Figure S7. Figure S7 shows that for any temperature T, both $\Delta F^{\mathrm{MBD}}(T)$ and $\Delta F^{\mathrm{SCAN}}(T)$ are on the same scale; only the zero-point energy is shifted (by 2.6 meV/atom) for the PBE + MBD calculation. Therefore, we expect the results of the PBE + MBD free energies to be comparable with nondispersion-corrected PBE free energies.

Using the MBD correction on black phosphorus in addition to the phonon modes of the previously mentioned phases of Cu−P, the hull in Figure 7a was constructed up to 600 K, above which no changes to stabilities are observed. A maximum value of 600 K was chosen so as not to approach the melting point of any phases, as the known phases of Cu−P typically have a melt between 800 and 1200 K. Furthermore, the harmonic approximation is a limited approach, and at higher temperatures, anharmonicity should be accounted for. $Fm\bar{3}m$−Cu_2P remains on the hull at 600 K, suggesting that it could be synthesized at high temperature. The convex hull is a confirmation that the $Cmc2_1$−Cu_8P_3 phase formed from two Cu vacancies in $P6_3cm$−Cu_3P is the more stable phase at room temperature, as at 300 K, $Cmc2_1$−Cu_8P_3 is within 10 meV/atom of the convex hull, as shown in Figure 7b. In addition, the destabilization of $I\bar{4}3d$−Cu_3P at high temperatures, shown in Figure 7b, suggests that this phase is not experimentally realizable and provides an explanation as to why it has not yet been experimentally synthesized. We can clearly see that $P6_3cm$−Cu_3P is stabilized at higher temperatures, as shown in Figure 7b, in which it is within 10 meV/atom of the convex hull at temperatures higher than 450 K.

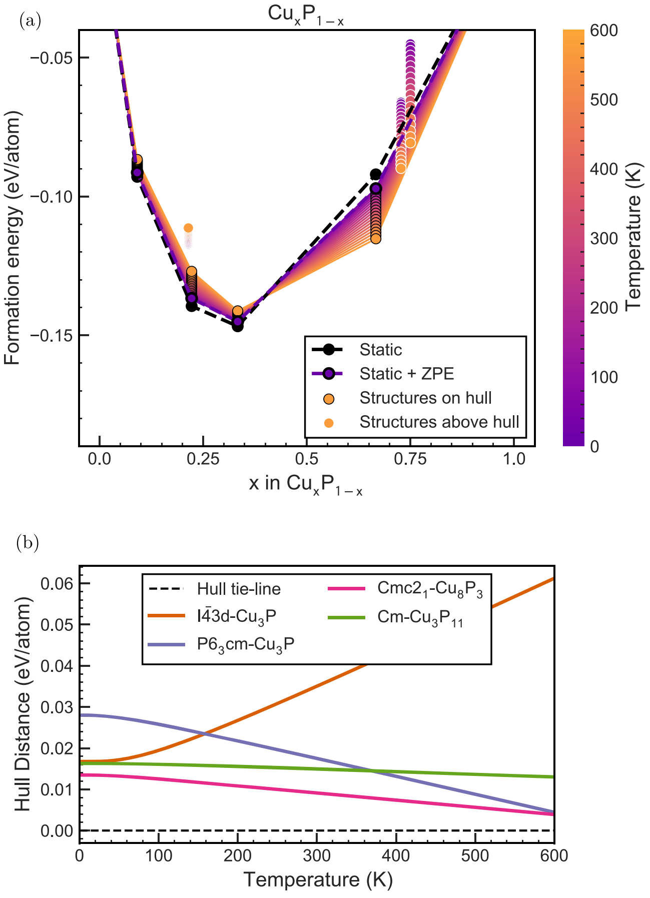

Figure 7. (a) Temperature-dependent convex hull with PBE *xc*-functional and MBD correction on the black phosphorus chemical potential. (b) Distance from the hull for the four structures that were above the convex hull tie-line at 0 K. All structures except $I\bar{4}3d$−Cu_3P get closer to the tie-line as the temperature increases, suggesting that they are stabilized by temperature. This agrees with the experimental evidence for Cu_8P_3 and $P6_3cm$−Cu_3P and suggests that Cu_3P_{11} may form experimentally.

Previous work on the $Cu_{3-x}P$ phases of $P6_3cm$−Cu_3P[47] confirms that the formation of two vacancies in Cu_3P is energetically stabilizing. By enumerating all of the possible structures with two Cu vacancies using the vacancy enumeration procedure described in the Methods section, we have determined that the $Cmc2_1$−Cu_8P_3 phase with two Cu vacancies in the 6c Wyckoff positions is the lowest-energy vacancy phase. Given the large number of ways to introduce these vacancies into the structure, configurational entropy will further stabilize this phase at high temperatures. To fully understand the nature of vacancy formation in $P6_3cm$−Cu_3P, a full cluster expansion could be performed, which is beyond the scope of this paper.

Cu_2P as a Li-Ion Battery Conversion Anode. $Fm\bar{3}m$−Cu_2P was computationally predicted to be energetically stable both as a 2D material[56] and now, in this article, as a bulk phase. The previous sections predict the stability of $Fm\bar{3}m$−Cu_2P at temperatures up to 600 K and characterize it as a metal with dispersive bands and delocalized conduction states at the Fermi level. An intuitive choice of application for Cu_2P lies in conversion anodes for Li-ion batteries, where previously both CuP_2 and Cu_3P were used as anodes with gravimetric capacities between 300 and 800 mAh/g.[11−14]

The crystal structure of $P6_3cm$−Cu_3P has a theoretical capacity of 363 mAh/g and experimentally has exhibited a range of capacities based upon the preparation method used.[13] The powdered Cu_3P anodes prepared by Bichat et al.[13] ranged in the initial capacity from 272 mAh/g using high-temperature synthesis in a silica tube to 527 mAh/g using low-temperature solvothermal synthesis. In the solvothermal route, the Cu_3P powders were prepared with copper chloride, water, and NH_4OH with white phosphorus, which could have resulted in copper oxide impurities leading to the initial capacity that is above the theoretical capacity of crystalline Cu_3P. Pfeiffer et al. synthesized Cu_3P powder by a solid-state reaction with red P in an ethanol suspension and Cu foil, and the initial capacity of Cu_3P was 415 mAh/g.[14] Energy-dispersive X-ray analysis showed that the stoichiometry was close to Cu_3P (though not exact), suggesting that this initial structure could have been within the stoichiometric range of $Cu_{3-x}P$ to achieve that initial capacity, in addition to the added capacity from likely oxide impurities.

In contrast, Cu_2P has a theoretical capacity of 509 mAh/g, which is above that of graphite at 372 mAh/g. The metallic nature of Cu_2P further enhances its use as a Li-ion battery anode, enabling fast electronic transfer through the electrode of the battery. In fact, Cu is already widely used as a current collector in contemporary Li-ion batteries, and previous studies on Cu_3P nanorods suggest that Cu−P anodes create a synergistic chemical interface with the Cu-current collector, which promotes cyclability.[15] Furthermore, because of its comparatively lower P content, volume changes during cycling are reduced, and therefore, the degradation is likely to be less severe.[12]

The volume expansion for a conversion anode with an overall conversion reaction

$$Cu_aP_b + 3bLi \rightarrow aCu + bLi_3P \quad (4)$$

is calculated as

$$\text{volume expansion}(\%) = 100 \times \left(\frac{b\,V(Li_3P) + a\,V(Cu)}{V(Cu_aP_b)} - 1\right) \quad (5)$$

where $V(Cu_aP_b)$ is the volume per formula unit of each phase in the conversion reaction. Using this equation, the volume expansion of $Fm\bar{3}m$−Cu_2P is 99%. This is comparable to the calculated volume expansion of $P6_3cm$−Cu_3P, which is 86%, and far superior to the volume expansion of CuP_2, which is 165%. The volume expansion for each binary Cu−P phase is shown in Figure S8, confirming that Cu_2P has the lowest volume expansion of the four stable phases on the convex hull. Experimental reports on the cycling of ball-milled CuP_2[12] suggest that volume expansion occurs, as after cycling for 10 cycles, the capacity is reduced by 50%, although they give no estimate of the level of volume expansion in the cell. The expansion is partially mitigated through the use of nanostructuring,[11] which allows cycling for 200 cycles. However, there is still capacity fading in this case, which reiterates the need for a high-capacity conversion anode with low-volume expansion, so as to reduce the need for nanostructuring or other postprocessing techniques to mitigate volume expansion. As both Cu_3P and Cu_2P have lower predicted volume expansions, and the synthesized Cu_3P shows no evidence of deleterious volume expansion,[13] it is likely that Cu_2P would also have minimal volume expansion in the experiment.

Using the convex hull constructed in Figure 1 and the structures on the ternary hull of Cu−Li−P, a voltage profile was constructed from the DFT ground-state energies for both $Fm\bar{3}m$−Cu_2P and $P6_3cm$−Cu_3P. All of the known ternary structures were included in this hull: $P\bar{3}m1$−Cu_2LiP, $I4/mmm$−Cu_2LiP_2, $Immm$−$Cu_4Li_5P_6$, and $Cmcm$−$CuLi_2P$, as well as the binary Li−P structures $Cmcm$-Li_3P, $P2_1/c$-LiP, $P2_12_12_1$-Li_3P_7, and $I4_1/acd$-LiP_7. A plane wave kinetic energy cutoff of 700 eV was used, and all structures on the hull were re-relaxed at this higher cutoff. The ternary hull is shown in Figure S9, in which the pathways from Cu−P to Li are also shown to depict how the voltage profiles for these Cu−P phases were calculated. The hull is shaded with a colormap to show the relative formation energy of phases on the hull, indicating that the Li−P phases have more negative formation energies (and thus create a deeper convex hull) than the Cu−P phases.

Although Cu−Li phases are predicted to be stable under the approximation of PBE, the formation energy of the predicted Cu_3Li phase is only 26 meV/atom in the OQMD database[19,64] and no phases of Cu−Li are predicted at finite temperature in the experiment.[65] Furthermore, Cu is used as a current collector in Li-ion batteries, specifically for its properties in resisting Li intercalation, and dead Li is found during cycling rather than Cu−Li phases.[66] Therefore, no Cu−Li compounds were included in the convex hull.

There are three ternary compounds on the Cu−Li−P hull in Figure S9; these are $I4/mmm$−Cu_2LiP_2, $Immm$−$Cu_4Li_5P_6$, and $Cmcm$−$CuLi_2P$. Experiments suggest that a hexagonal $LiCu_2P$ phase forms[67] during cycling; however, the $P\bar{3}m1$−Cu_2LiP (ICSD 659706)[46] phase of this structure is 39 meV/atom above the hull at a plane wave cutoff of 700 eV.

From this ternary hull, shown in Figure S9, the voltage profile shown in Figure 8 was constructed. This hull is calculated as usual, without incorporating vibrational effects at 0 K. As the

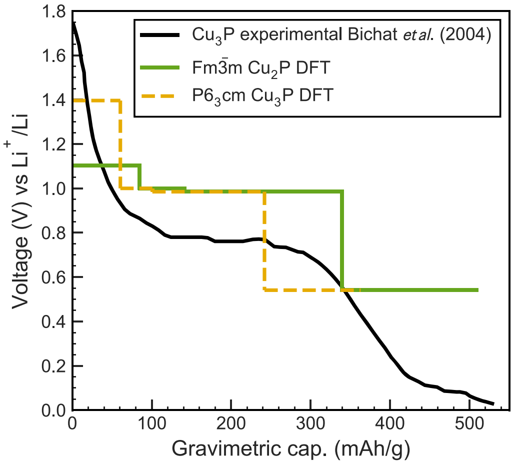

Figure 8. Ground-state voltage profile for $Fm\bar{3}m$−Cu_2P and $P6_3cm$−Cu_3P generated from the DFT ground-state structures of Cu−Li−P. The experimental profile was adapted from ref 67. The experimental onset voltage matches closely with Cu_3P and shows a similar capacity to Cu_2P, though this added capacity is likely due to oxide impurities in the experiment.

$P\bar{3}m1{-}Cu_2LiP$ phase suggested in the experiment[46,67] is 39 meV/atom above the convex hull, it cannot be in the voltage profile calculated in Figure 8. The 0 K voltage profile includes the $I4/mmm{-}Cu_2LiP_2$ phase, which has been previously synthesized through a solid-state reaction,[68] and is a high T_c pnictide superconductor.[69] The $I4/mmm{-}Cu_2LiP_2$ phase has not, to our knowledge, been identified during cycling in Li-ion batteries previously.

Both Cu_2P and Cu_3P have the same overall reaction mechanism given by eq 4, and the stable phases during the reaction from charging Cu_3P are given in Table 2. These reactions show that Cu_2P operates in a narrower voltage window than Cu_3P and has a higher predicted gravimetric capacity. The predicted structures forming at each capacity and voltage are given in the 4th column of Table 2. Though $Fm\bar{3}m{-}Cu_2P$ undergoes the same lithiation process as $P6_3cm{-}Cu_3P$, $Fm\bar{3}m{-}Cu_2P$ has a higher capacity of 508 mAh/g and a higher average voltage of 0.86 V versus Li/Li$^+$, while $P6_3cm{-}Cu_3P$ has a capacity of 363 mAh/g and an average voltage of 0.91 V.

Table 2. Reaction Pathways for $Cu_nP + Li \rightarrow Li_3P + nCu$

reaction stage	gravimetric capacity (mAh/g)	voltage (V)	reaction pathway
	$Cu_2P + 3Li \rightarrow Li_3P + 2Cu$		
I	85	1.10	$1/2Cu_2LiP_2 + Cu$
II	141	1.00	$1/6Cu_4Li_5P_6 + 4/3Cu$
III	338	0.98	$CuLi_2P + Cu$
IV	509	0.54	$Li_3P + 2Cu$
	$Cu_3P + 3Li \rightarrow Li_3P + 3Cu$		
I	60	1.53	$1/2Cu_2LiP_2 + 2Cu$
II	101	1.00	$1/6Cu_4Li_5P_6 + 7/3Cu$
III	242	0.98	$CuLi_2P + 2Cu$
IV	363	0.54	$Li_3P + 3Cu$

Each plateau in the ground-state voltage profile in Figure 8 represents a three-phase region of the ternary hull in which phases of Cu−Li−P are stable. Here, Cu_3P was "stabilized" on the ternary hull by artificially excluding the $CuP_2{-}Cu_2P_7$ and Cu_2P phases. This is an approximation of a convex hull in which Cu_3P is on the tie-line, which does not affect the formation energy (and thus predicted voltages) of the other phases. The experimental voltage curve shown in Figure 8 from ref 67 exhibits a similar trend in phase transitions along the cycle as the theoretical curve for Cu_3P.

■ CONCLUSIONS

Using four different computational crystal structure-searching techniques on the copper phosphides, several structures that lie close to the convex hull (within 20 meV/atom) were predicted, including $Cm{-}Cu_3P_{11}$, $I\bar{4}3d{-}Cu_3P$, and $Fm\bar{3}m{-}Cu_2P$; the experimentally characterized $P\bar{1}{-}CuP_{10}$, $C2/m{-}Cu_2P_7$, and $P2_1/c{-}CuP_2$ were all on the convex hull tie-line. By calculating the phonon dispersion curves of all structures within 20 meV/atom of the Cu−P convex hull, we constructed a temperature-dependent convex hull that predicted $Fm\bar{3}m{-}Cu_2P$ to be stable up to 600 K, while $I\bar{4}3d{-}Cu_3P$ was destabilized with increasing temperature. We have also shown that the $Cmc2_1{-}Cu_8P_3$ phase formed from two Cu vacancies at the 6c Wyckoff positions of $P6_3cm{-}Cu_3P$ is stabilized with increasing temperature and is within 10 meV/atom of the convex hull above 300 K. Experimental diffractometry on single crystals of Cu_3P suggests that the phase has a range of stoichiometries between $Cu_{2.6}P$ and $Cu_{2.8}P$,[43,47] and Cu_8P_3 (or $Cu_{2.67}P$ equivalently) is within these bounds.

In addition to confirming the stability of $Cmc2_1{-}Cu_8P_3$, we also confirmed that $Cm{-}Cu_3P_{11}$ remains metastable up to high temperatures, as shown in the temperature-dependent hull in Figure 7. While Cu_3P_{11} is unlikely to be used as a Li-ion battery anode, given its high P content, and therefore susceptibility to volume expansion, it could be a novel phase to consider within the Cu−P phase diagram. CuP_{10} was identified experimentally by preparing Cu_2P_7 in excess P;[70] given the structural similarity between $Cm{-}Cu_3P_{11}$ and $C2/m{-}Cu_2P_7$ shown in Figure 2, it is possible that $Cm{-}Cu_3P_{11}$ is also formed in excess P. Using the PXRD patterns presented in Figure 3, it may be possible to distinguish the $Cm{-}Cu_3P_{11}$ phase from $C2/m{-}Cu_2P_7$ experimentally, from the change in the peak intensity at 16° and peak differences at 2θ values $< 20°$; however, further experimental analysis is likely required given the low intensity of this peak.

Finally, $Fm\bar{3}m{-}Cu_2P$ is the only phase identified through crystal structure prediction, which was found on the hull at 0 K and which remained on the convex hull at finite temperature, strongly suggesting that it is possible to synthesize Cu_2P experimentally. Furthermore, its synthesis could provide a novel conversion anode, with favorable properties for Li-ion batteries. Hybrid functional calculations of the electronic properties of Cu_2P predict it to be isostructural and qualitatively similar electronically to both Rh_2P and Ir_2P, which are also $Fm\bar{3}m$ metals with dispersive bands at the Fermi level. This was confirmed using spin-polarized calculations, with both vector and scalar spin treatments, hybrid functional calculations using the HSE06 functional, and finally a projected band structure and density of states using PBE. This confirmation of the metallic nature of Cu_2P using a wide range of functionals and spin treatments suggests that this could be a better choice for anode than Li−P, which are insulators with wide band gaps. Furthermore, the presence of such dispersive bands suggests high electron mobility within the anode, which would mitigate fast charge transfer between the Cu current collector and Li-ions. Finally, given its higher capacity (509 mAh/g) compared to Cu_3P, Cu_2P has potential as an experimentally realizable conversion anode, which has a capacity that is competitive with graphite, conductive to promote electronic transfer within the anode, and less vulnerable to degradation compared to high P content conversion anodes due to reduced levels of cyclic volume changes.

■ ASSOCIATED CONTENT

SI Supporting Information

The Supporting Information is available free of charge at https://pubs.acs.org/doi/10.1021/acs.chemmater.0c02054.

The input and output files associated with our calculations have been deposited into the Cambridge Repository at https://doi.org/10.17863/CAM.54795 in the Cambridge Repository; and all analysis is on GitHub at harpaf13/data.copper-phosphides and Binder.

> Details of the simulation of powder X-ray diffraction patterns and pair distribution functions, as well as the electronic band structure calculations using spin−orbit coupling (PDF)

AUTHOR INFORMATION

Corresponding Author

Andrew J. Morris − *School of Metallurgy and Materials, University of Birmingham, Edgbaston, Birmingham B15 2TT, U.K.;* orcid.org/0000-0001-7453-5698;
Email: a.j.morris.1@bham.ac.uk

Authors

Angela F. Harper − *Theory of Condensed Matter, Cavendish Laboratory, University of Cambridge, Cambridge CB3 0HE, U.K.;* orcid.org/0000-0002-0699-0450

Matthew L. Evans − *Theory of Condensed Matter, Cavendish Laboratory, University of Cambridge, Cambridge CB3 0HE, U.K.;* orcid.org/0000-0002-1182-9098

Complete contact information is available at:
https://pubs.acs.org/10.1021/acs.chemmater.0c02054

Notes

The authors declare no competing financial interest.

ACKNOWLEDGMENTS

The authors would like to thank Bartomeu Monserrat for his discussions on the electronic structure and Matthew Cliffe for his discussions on PXRD. The authors would also like to thank Can Koçer for looking over the manuscript text. A.F.H. acknowledges the financial support of the Gates Cambridge Trust and the Winton Programme for the Physics of Sustainability, University of Cambridge, U.K. M.L.E. acknowledges the Engineering and Physical Sciences Research Council (EPSRC) Centre for Doctoral Training in Computational Methods for Materials Science, U.K., for funding (EP/L015552/1). A.J.M. acknowledges funding from EPSRC (EP/P003532/1). The authors acknowledge networking support via the EPSRC Collaborative Computational Projects, CCP9 (EP/M022595/1) and CCP-NC (EP/T026642/1). This work was performed using resources provided by the Cambridge Service for Data Driven Discovery (CSD3) operated by the University of Cambridge Research Computing Service (www.csd3.cam.ac.uk), provided by Dell EMC and Intel, using Tier-2 funding from the Engineering and Physical Sciences Research Council (capital grant EP/P020259/1), and DiRAC funding from the Science and Technology Facilities Council (www.dirac.ac.uk).

ADDITIONAL NOTE

[a] OTF pseudopotential strings are Cu: 3|2.2|2.0|1.0|10|12|13|40:41:32(qc=6), P: 3|1.8|4|4|5|30:31:32, and Li: 1|1.0|14|16|18|10U:20(qc=7).

REFERENCES

(1) Ramireddy, T.; Xing, T.; Rahman, M. M.; Chen, Y.; Dutercq, Q.; Gunzelmann, D.; Glushenkov, A. M. Phosphorus-carbon nanocomposite anodes for lithium-ion and sodium-ion batteries. *J. Mater. Chem. A* **2015**, *3*, 5572−5584.

(2) Bhatt, M. D.; Lee, J. Y. High capacity conversion anodes in Li-ion batteries: A review. *Int. J. Hydrogen Energy* **2019**, *44*, 10852−10905.

(3) Tarascon, J.-M.; Armand, M. Issues and challenges facing rechargeable lithium batteries. *Nature* **2001**, *414*, 359−367.

(4) Kirklin, S.; Meredig, B.; Wolverton, C. High-throughput computational screening of new Li-ion battery anode materials. *Adv. Energy Mater.* **2013**, *3*, 252−262.

(5) Sun, M.; Liu, H.; Qu, J.; Li, J. Earth-rich transition metal phosphide for energy conversion and storage. *Adv. Energy Mater.* **2016**, *6*, No. 1600087.

(6) Feng, L.; Xue, H. Advances in transition-metal phosphide applications in electrochemical energy storage and catalysis. *ChemElectroChem* **2017**, *4*, 20−34.

(7) Lu, Y.; Yu, L.; Lou, X. W. D. Nanostructured conversion-type anode materials for advanced lithium-ion batteries. *Chem* **2018**, *4*, 972−996.

(8) Boyanov, S.; Bernardi, J.; Gillot, F.; Dupont, L.; Womes, M.; Tarascon, J.-M.; Monconduit, L.; Doublet, M.-L. FeP: Another attractive anode for the Li-ion battery enlisting a reversible two-step insertion/conversion process. *Chem. Mater.* **2006**, *18*, 3531−3538.

(9) Zhang, Y.; Zhang, H.; Feng, Y.; Liu, L.; Wang, Y. Unique Fe_2P nanoparticles enveloped in sandwichlike graphited carbon sheets as excellent hydrogen evolution reaction catalyst and Lithium-ion battery anode. *ACS Appl. Mater. Interfaces* **2015**, *7*, 26684−26690.

(10) Lu, Y.; Wang, X.; Mai, Y.; Xiang, J.; Zhang, H.; Li, L.; Gu, C.; Tu, J.; Mao, S. X. Ni_2P/graphene sheets as anode materials with enhanced electrochemical properties versus lithium. *J. Phys. Chem. C* **2012**, *116*, 22217−22225.

(11) Kim, S.-O.; Manthiram, A. Phosphorus-rich CuP_2 embedded in carbon matrix as a high-performance anode for Li-ion batteries. *ACS Appl. Mater. Interfaces* **2017**, *9*, 16221−16227.

(12) Wang, K.; Yang, J.; Xie, J.; Wang, B.; Wen, Z. Electrochemical reactions of lithium with CuP_2 and $Li_{1.75}Cu_{1.25}P_2$ synthesized by ballmilling. *Electrochem. Commun.* **2003**, *5*, 480−483.

(13) Bichat, M.-P.; Politova, T.; Pfeiffer, H.; Tancret, F.; Monconduit, L.; Pascal, J.-L.; Brousse, T.; Favier, F. Cu_3P as anode material for lithium ion battery: powder morphology and electrochemical performances. *J. Power Sources* **2004**, *136*, 80−87.

(14) Pfeiffer, H.; Tancret, F.; Bichat, M.-P.; Monconduit, L.; Favier, F.; Brousse, T. Air stable copper phosphide (Cu_3P): a possible negative electrode material for lithium batteries. *Electrochem. Commun.* **2004**, *6*, 263−267.

(15) Villevieille, C.; Robert, F.; Taberna, P. L.; Bazin, L.; Simon, P.; Monconduit, L. The good reactivity of lithium with nanostructured copper phosphide. *J. Mater. Chem.* **2008**, *18*, 5956−5960.

(16) Ni, S.; Ma, J.; Lv, X.; Yang, X.; Zhang, L. The fine electrochemical performance of porous Cu_3P/Cu and the high energy density of Cu_3P as anode for Li-ion batteries. *J. Mater. Chem. A* **2014**, *2*, 20506−20509.

(17) Chandrasekar, M.; Mitra, S. Thin copper phosphide films as conversion anode for lithium-ion battery applications. *Electrochim. Acta* **2013**, *92*, 47−54.

(18) Curtarolo, S.; Setyawan, W.; Hart, G. L.; Jahnatek, M.; Chepulskii, R. V.; Taylor, R. H.; Wang, S.; Xue, J.; Yang, K.; Levy, O.; Mehl, M. J.; Stokes, H. T.; Demchenko, D. O.; Morgan, D. AFLOW: An automatic framework for high-throughput materials discovery. *Comput. Mater. Sci.* **2012**, *58*, 218−226.

(19) Saal, J. E.; Kirklin, S.; Aykol, M.; Meredig, B.; Wolverton, C. Materials design and discovery with high-throughput density functional theory: the open quantum materials database (OQMD). *JOM* **2013**, *65*, 1501−1509.

(20) Hautier, G.; Fischer, C.; Ehrlacher, V.; Jain, A.; Ceder, G. Data mined ionic substitutions for the discovery of new compounds. *Inorg. Chem.* **2011**, *50*, 656−663.

(21) Evans, M. *GitHub*, matador v0.9, 2020. https://doi.org/10.5281/zenodo.3908573 (accessed May 11, 2020).

(22) Evans, M. *GitHub*, ilustrado v0.3, 2020. https://zenodo.org/record/3904495 (accessed May 11, 2020).

(23) Harper, A. F.; Evans, M. L.; Darby, J. P.; Karasulu, B.; Koçer, C. P.; Nelson, J. R.; Morris, A. J. Ab initio structure prediction methods for battery materials. *Johnson Matthey Technol. Rev.* **2019**, *64*, 103−118.

(24) See, K. A.; Leskes, M.; Griffin, J. M.; Britto, S.; Matthews, P. D.; Emly, A.; Van der Ven, A.; Wright, D. S.; Morris, A. J.; Grey, C. P.; et al. Ab initio structure search and in situ ^{7}Li NMR studies of discharge products in the Li-S battery system. *J. Am. Chem. Soc.* **2014**, *136*, 16368−16377.

(25) Mayo, M.; Morris, A. J. Structure prediction of Li-Sn and Li-Sb intermetallics for lithium-ion batteries anodes. *Chem. Mater.* **2017**, *29*, 5787−5795.

(26) Mayo, M.; Griffith, K. J.; Pickard, C. J.; Morris, A. J. Ab initio study of phosphorus anodes for lithium and sodium-ion batteries. *Chem. Mater.* **2016**, *28*, 2011−2021.

(27) Marbella, L. E.; Evans, M. L.; Groh, M. F.; Nelson, J.; Griffith, K. J.; Morris, A. J.; Grey, C. P. Sodiation and desodiation via helical phosphorus intermediates in highcapacity anodes for sodium-ion batteries. *J. Am. Chem. Soc.* **2018**, *140*, 7994−8004.

(28) Hellenbrandt, M. The inorganic crystal structure database (ICSD)—present and future. *Crystallogr. Rev.* **2004**, *10*, 17−22.

(29) Pickard, C. J.; Needs, R. Ab initio random structure searching. *J. Phys. Condens. Matter* **2011**, *23*, No. 053201.

(30) Deaven, D. M.; Ho, K. M. Molecular Geometry Optimization with a Genetic Algorithm. *Phys. Rev. Lett.* **1995**, *75*, 288−291.

(31) Clark, S. J.; Segall, M. D.; Pickard, C. J.; Hasnip, P. J.; Probert, M. I.; Refson, K.; Payne, M. C. First principles methods using CASTEP. *Z. Kristallogr. - Cryst. Mater.* **2005**, *220*, 567−570.

(32) Perdew, J. P.; Burke, K.; Ernzerhof, M. Generalized gradient approximation made simple. *Phys. Rev. Lett.* **1996**, *77*, 3865.

(33) Vanderbilt, D. Soft self-consistent pseudopotentials in a generalized eigenvalue formalism. *Phys. Rev. B* **1990**, *41*, 7892.

(34) Sun, L.-Q.; Li, M.-J.; Sun, K.; Yu, S.-H.; Wang, R.-S.; Xie, H.-M. Electrochemical activity of black phosphorus as an anode material for lithium-ion batteries. *J. Phys. Chem. C* **2012**, *116*, 14772−14779.

(35) Urban, A.; Seo, D.-H.; Ceder, G. Computational understanding of Li-ion batteries. *npj Comput. Mater.* **2016**, *2*, 1−13.

(36) Hinuma, Y.; Pizzi, G.; Kumagai, Y.; Oba, F.; Tanaka, I. Band structure diagram paths based on crystallography. *Comput. Mater. Sci.* **2017**, *128*, 140−184.

(37) Togo, A.; Tanaka, I. Spglib: A Software Library for Crystal Symmetry Search. 2018, arXiv:1808.01590. arXiv.org e-Print archive. http://arxiv.org/abs/1808.01590 (accessed Feb 19, 2020).

(38) Morris, A. J.; Nicholls, R. J.; Pickard, C. J.; Yates, J. R. OptaDOS: A tool for obtaining density of states, core-level and optical spectra from electronic structure codes. *Comput. Phys. Commun.* **2014**, *185*, 1477−1485.

(39) Nicholls, R. J.; Morris, A. J.; Pickard, C. J.; Yates, J. R. Accurate and efficient method for many-body van der Waals interactions. *J. Phys.: Conf. Ser.* **2012**, No. 012062.

(40) Tkatchenko, A.; DiStasio, R. A., Jr.; Car, R.; Scheffler, M. OptaDOS—a new tool for EELS calculations. Journal of Physics Conference Series. *Phys. Rev. Lett.* **2012**, *108*, No. 236402.

(41) Sun, W.; Dacek, S. T.; Ong, S. P.; Hautier, G.; Jain, A.; Richards, W. D.; Gamst, A. C.; Persson, K. A.; Ceder, G. The thermodynamic scale of inorganic crystalline metastability. *Sci. Adv.* **2016**, *2*, No. e1600225.

(42) Zhang, G.-X.; Reilly, A. M.; Tkatchenko, A.; Scheffler, M. Performance of various density-functional approximations for cohesive properties of 64 bulk solids. *New J. Phys.* **2018**, *20*, No. 063020.

(43) Olofsson, O. The crystal structure of Cu_3P. *Acta Chem. Scand.* **1972**, *26*, 2777−2787.

(44) Lange, S.; Bawohl, M.; Weihrich, R.; Nilges, T. Mineralization Routes to Polyphosphides: Cu_2P_{20} and Cu_5InP_{16}. *Angew. Chem., Int. Ed.* **2008**, *47*, 5654−5657.

(45) Møuller, M.; Jeitschko, W. Representation, properties and crystal structure of Cu_2P_7 and structure refinements of CuP_2 and AgP_2. *J. Inorg. Gen. Chem.* **1982**, *491*, 225−236.

(46) Schlenger, H.; Jacobs, H.; Juza, R. Ternary phases of lithium with copper and phosphorus. *J. Inorg. Gen. Chem.* **1971**, *385*, 177−201.

(47) De Trizio, L.; Gaspari, R.; Bertoni, G.; Kriegel, I.; Moretti, L.; Scotognella, F.; Maserati, L.; Zhang, Y.; Messina, G. C.; Prato, M.; et al. $Cu_{3-x}P$ nanocrystals as a material platform for near-infrared plasmonics and cation exchange reactions. *Chem. Mater.* **2015**, *27*, 1120−1128.

(48) Otte, H. M. Lattice parameter determinations with an x-ray spectrogoniometer by the debye-scherrer method and the effect of specimen condition. *J. Appl. Phys.* **1961**, *32*, 1536−1546.

(49) Steenberg, B. *The Crystal Structure of Cu_3As and Cu_3P*; Almqvist & Wiksell, 1938; Vol. *12*.

(50) Owusu, M.; Jawad, H.; Lundström, T.; Rundqvist, S. Crystallographic Studies of Cr_3P and of the Solid Solution of Hydrogen in Zr_3P. *Phys. Scr.* **1972**, *6*, 67−70.

(51) Zumbusch, M. On the structures of uranium sulfide and subphosphide of iridium and rhodium. *J. Inorg. Gen. Chem.* **1940**, *243*, 322−329.

(52) Moeller, M. H.; Jeitschko, W. Preparation and crystal structure of trisilver undecaphosphide, Ag_3P_{11}, an unusual defect tetrahedral compound. *Inorg. Chem.* **1981**, *20*, 828−833.

(53) Crichton, W. A.; Mezouar, M.; Monaco, G.; Falconi, S. Phosphorus: New in situ powder data from large-volume apparatus. *Powder Diffr.* **2003**, *18*, 155−158.

(54) Thurn, H.; Krebs, H. Über Struktur und Eigenschaften der Halbmetalle. XXII. Die Kristallstruktur des Hittorfschen Phosphors. *Acta Crystallogr., Sect. B: Struct. Crystallogr. Cryst. Chem.* **1969**, *25*, 125−135.

(55) Wolff, A.; Doert, T.; Hunger, J.; Kaiser, M.; Pallmann, J.; Reinhold, R.; Yogendra, S.; Giebeler, L.; Sichelschmidt, J.; Schnelle, W.; et al. Low-Temperature Tailoring of Copper-Deficient $Cu_{3-x}P$—Electric Properties, Phase Transitions, and Performance in Lithium-Ion Batteries. *Chem. Mater.* **2018**, *30*, 7111−7123.

(56) Yang, L.-M.; Ganz, E. Adding a new dimension to the chemistry of phosphorus and arsenic. *Phys. Chem. Chem. Phys.* **2016**, *18*, 17586−17591.

(57) Iglesias, J.; Nowacki, W. Refinement of the crystal structure of α domeykite, a structure related to the A15 type. *Z. Kristallogr. - Cryst. Mater.* **1977**, *145*, 334−345.

(58) Rundqvist, S. Phosphides of the platinum metals. *Nature* **1960**, *185*, 31−32.

(59) Jain, A.; Ong, S. P.; Hautier, G.; Chen, W.; Richards, W. D.; Dacek, S.; Cholia, S.; Gunter, D.; Skinner, D.; Ceder, G.; Persson, K. A. The Materials Project: A materials genome approach to accelerating materials innovation. *APL Mater.* **2013**, *1*, No. 011002.

(60) Larsson, E. An X-ray investigation of the Ni-P system and the crystal structures of NiP and NiP_2. *Ark. Kemi* **1965**, *23*, 335−365.

(61) Carlsson, B.; Gölin, M.; Rundqvist, S. Determination of the homogeneity range and refinement of the crystal structure of Fe_2P. *J. Solid State Chem.* **1973**, *8*, 57−67.

(62) Song, M.-S.; Kang, Y.-M.; Kim, Y.-I.; Park, K.-S.; Kwon, H.-S. Nature of insulatingphase transition and degradation of structure and electrochemical reactivity in an olivine-structured material, $LiFePO_4$. *Inorg. Chem.* **2009**, *48*, 8271−8275.

(63) Baroni, S.; de Gironcoli, S.; Dal Corso, A.; Giannozzi, P. Phonons and related crystal properties from density-functional perturbation theory. *Rev. Mod. Phys.* **2001**, *73*, 515−562.

(64) Van de Walle, A.; Moser, Z.; Gasior, W. First-principles calculation of the Cu-Li phase diagram. *Arch. Metall.* **2004**, *49*, 535−544.

(65) Okamoto, H. Cu-Li (copper-lithium). *J. Phase Equilib. Diffus.* **2011**, *32*, 172.

(66) Fang, C.; Li, J.; Zhang, M.; Zhang, Y.; Yang, F.; Lee, J. Z.; Lee, M.-H.; Alvarado, J.; Schroeder, M. A.; Yang, Y.; et al. Quantifying inactive lithium in lithium metal batteries. *Nature* **2019**, *572*, 511−515.

(67) Bichat, M. P.; Politova, T.; Pascal, J. L.; Favier, F.; Monconduit, L. Electrochemical Reactivity of Cu_3P with Lithium. *J. Electrochem. Soc.* **2004**, *151*, A2074.

(68) Schlenger, H.; Jacobs, H. Die Kristallstrukturen des $LiCu_2P_2$ und des $Li_{1.75}Cu_{1.25}P_2$. *Acta Crystallogr., Sect. B: Struct. Crystallogr. Cryst. Chem.* **1972**, *28*, 327.

(69) Han, J.-T.; Zhou, J.-S.; Cheng, J.-G.; Goodenough, J. B. A new pnictide superconductor without iron. *J. Am. Chem. Soc.* **2010**, *132*, 908−909.

(70) Bawohl, M.; Nilges, T. Phosphorus rich d^{10} ion polyphosphides and selected materials. *Z. Anorg. Allg. Chem.* **2015**, *641*, 304−310.